EARTHQUAKES

Hierarchical interlocked orthogonal faulting in the 2019 Ridgecrest earthquake sequence

Zachary E. Ross[1]*, Benjamín Idini[1], Zhe Jia[1], Oliver L. Stephenson[1], Minyan Zhong[1], Xin Wang[1], Zhongwen Zhan[1], Mark Simons[1], Eric J. Fielding[2], Sang-Ho Yun[2], Egill Hauksson[1], Angelyn W. Moore[2], Zhen Liu[2], Jungkyo Jung[2]

A nearly 20-year hiatus in major seismic activity in southern California ended on 4 July 2019 with a sequence of intersecting earthquakes near the city of Ridgecrest, California. This sequence included a foreshock with a moment magnitude (M_w) of 6.4 followed by a M_w 7.1 mainshock nearly 34 hours later. Geodetic, seismic, and seismicity data provided an integrative view of this sequence, which ruptured an unmapped multiscale network of interlaced orthogonal faults. This complex fault geometry persists over the entire seismogenic depth range. The rupture of the mainshock terminated only a few kilometers from the major regional Garlock fault, triggering shallow creep and a substantial earthquake swarm. The repeated occurrence of multifault ruptures, as revealed by modern instrumentation and analysis techniques, poses a formidable challenge in quantifying regional seismic hazards.

Over the past three decades, an increasing number of well-documented earthquakes have ruptured multiple faults (*1*–*5*), highlighting the importance of incorporating this geometric complexity into models of seismic hazard. On 4 July 2019, a sequence of damaging earthquakes began near the city of Ridgecrest, California, and activated a complex fault network, further illustrating the need to understand how multiple faults can rupture in a single earthquake.

The Ridgecrest sequence included a foreshock with a moment magnitude (M_w) of 6.4 followed by an M_w 7.1 mainshock nearly 34 hours later (Fig. 1). These dominantly strike-slip earthquakes occurred on largely unmapped faults that cumulatively extend more than 75 km in length. Shaking from these events was felt throughout portions of California, Nevada, and even Arizona. Damage was primarily concentrated in the towns of Ridgecrest and Trona. The severity of damage was limited, as the area is sparsely populated. However, substantial portions of the ruptures occurred within the boundaries of the Naval Air Weapons Station at China Lake and caused major damage to facilities there.

Seismic activity occurred within the Little Lake fault zone (LLFZ) and nearby Airport Lake fault zone, both of which have a long history of activity (Fig. 1), including multiple sequences with M_w of >5 between 1982 and 1996 (*6*). The LLFZ is accumulating right-lateral strain of about 1 mm/year (*7*) and is bounded to the southeast by the Garlock fault, a 260-km-long left-lateral strike-slip fault capable of producing M_w ~7.8 earthquakes (*8*). The Coso geothermal area abuts the LLFZ to the northwest and is the site of one of the largest geothermal power plants in the United States. Numerous earthquake swarms have occurred in this area (*9*). To the northwest of Coso is the southern terminus of the 1872 M_w 7.5 Owens Valley earthquake (*10*) (Fig. 1), which is among the largest historical earthquakes in California and was responsible for 27 deaths.

In the time since the last major earthquake in California, the quality of seismic and geodetic data available has improved substantially. The Southern California Seismic Network has nearly doubled in size, Global Positioning System (GPS) stations have been installed throughout the region, and interferometric synthetic aperture radar (InSAR) data are available at unprecedented levels of quality with shorter times between acquisitions. Here, we analyze these datasets with state-of-the-art techniques, including a high-resolution seismicity catalog derived from template matching, detailed multifault inversions of geodetic data with nonplanar geometry, and subevent modeling of the largest events in the sequence. The observations indicate that the Ridgecrest sequence ruptured an astonishingly complex network of intertwined orthogonal faults operating over a broad range of length scales. They also show that the Garlock fault experienced shallow triggered postseismic creep and a large earthquake swarm; the role this major tectonic structure plays in limiting the southern extent of faulting and seismicity is yet to be understood.

The 2019 Ridgecrest sequence

The Ridgecrest mainshock was preceded by a prominent foreshock sequence that began with numerous events of local magnitude (M_L) ~0 (Fig. 1). The seismicity rates escalated rapidly, with an M_w 4 event 2 hours later and an M_w 6.4 earthquake shortly thereafter. Over the first 21 days of the sequence, more than 111,000 earthquakes with M of >0.5 occurred, including 70 events with an M of >4.

To resolve the geometry of the fault zone that ruptured during the Ridgecrest sequence, we produced a comprehensive relocated seismicity catalog with template matching that had nominal relative resolution of ~100 m horizontally and 350 m vertically (*11*) (Fig. 2). We paired this catalog with a damage proxy map (DPM) (*11*) (Fig. 3), extracted from satellite InSAR coherence data, that identifies regions where radar-scattering properties of the ground have changed substantially relative to their inherent background rates of change (*12*). The fault zone exhibits pervasive orthogonal faulting over multiple length scales with notable geometric complexity (Figs. 2 and 3). The largest scale is for a roughly 55-km-long northwest-striking structure with an undulating geometry that is orthogonally cross-cut by a ~15-km-long fault. The larger of these was the primary structure that ruptured during the M_w 7.1 earthquake, while the smaller structure was the largest that ruptured during the M_w 6.4 event (Fig. 3).

Around the northwest rupture terminus, the main fault dips steeply to the southwest before transitioning to a northeast dip of roughly 70° on the segment of the fault southeast of the M_w 7.1 hypocenter. Toward the southeast part of the rupture, the largest fault bifurcates into two subparallel strands that are separated by 7 km and that continue for about 12 km each (Figs. 2 and 3). Near the main intersection of the M_w 7.1 and M_w 6.4 ruptures, there are at least 20 orthogonal faults that appear as lineations in the seismicity and features in the DPM. The lineations often localize to a width of roughly 100 to 200 m, which is comparable to the uncertainty of the hypocenter locations (*11*). The general absence of orthogonal faulting in the northwest section of the rupture may indicate that this part of the fault zone is slightly further along in the evolutionary process. Numerous horsetail structures are oriented at an oblique angle to the main rupture trace at the northwest rupture terminus.

Nearly all of the geometric features described are present in the seismicity as well as the InSAR surface deformation, indicating that they are representative of the fault structure over the entire seismogenic zone. As defined by seismicity, the bottom of the seismogenic zone lies around 10 km at its deepest extent, with the maximum depth slowly decreasing to about 5 km toward the southeast (Fig. 2). Such a shallow seismogenic zone is also present in the Salton Trough region of California and is often attributed to the elevated heat flow (*13*); similar heat flow anomalies exist near the Ridgecrest sequence (*14*) and may control the boundaries of the brittle-ductile transition zone.

On the basis of kinematic subevent inversion of seismograms from the dense regional seismic network and global seismic stations, the M_w 6.4 earthquake had a duration of about

[1]Seismological Laboratory, California Institute of Technology, Pasadena, CA 91125, USA. [2]Jet Propulsion Laboratory, California Institute of Technology, Pasadena, CA 91109, USA.
*Corresponding author. Email: zross@caltech.edu

12 s, with three subevents best explaining the data (Fig. 4). These three subevents coincide with at least three faults. The 6-km-long northwest-trending fault slipped first, with an equivalent M_w 6.1 (subevent E1). This is consistent with the hypocenter of this event, which is located about 2 km northwest of the long southwest trending fault. Thus, a rupture propagated over a short southwest-trending fault with only about 5 km of surface break, yet the equivalent magnitude for this segment, was the M_w 6.2 subevent (E2). Our analysis of this subevent indicates that it is required by the data and that the magnitude is well resolved (figs. S1 to S4). However, this subevent may also include slip on an adjacent northwest-trending orthogonal fault. Because the seismicity on the E2 segment extends across the main fault of the mainshock (Fig. 2), part of the slip probably occurred on the other side, but only at depth. The rupture then jumped to a larger southwest-trending fault that is about 15 km long, producing again an equivalent seismic moment to an M_w 6.2 earthquake (E3) and a large surface rupture.

Additional insights into the rupture process of the M_w 6.4 earthquake are given by a joint inversion of the geodetic data spanning both events and constraints provided by the relocated seismicity (Fig. 5 and fig. S10). On the faults closest to the three kinematic subevents, there is appreciable slip in our model. This event nucleated at the intersection between two faults trending northwest and southwest (Fig. 5). The 15-km-long southwest-oriented left-lateral fault that aligns with subevent E3 (Fig. 4) produced a maximum of about 5 m slip. The large slip patches on these faults are coincident with regions of decreased aftershock density (fig. S10).

Our kinematic subevent model of the M_w 7.1 mainshock shows that the rupture lasted for about 22 s and can be explained by four subevents (Fig. 4). The initial 5 s of the rupture had little moment, whereas the subevent with the largest moment (subevent E1, M_w 6.9) occurred close to the hypocenter between 5 and 10 s. This subevent appears to have ruptured bilaterally, given its large seismic moment. Centroid locations of the later subevents propagated very slowly to the southeast, suggesting a unilateral rupture. The final subevent, E4 (at 20 s), occurred ~25 km southeast of the first subevent E1 (at 7 s), indicating a slow average rupture velocity of roughly 2 km/s.

The M_w 7.1 earthquake nucleated about 10 km to the northwest of the M_w 6.4 event and ruptured a fault network with a cumulative length of about 65 km. Most of the slip occurred near the hypocenter (Fig. 5), where an ~30-km-long patch produced a maximum of about 9 m slip at the scales resolved by our model. This part of the rupture is notably deficient in aftershocks relative to the rest of the rupture (fig. S10), a feature that is common to large slip

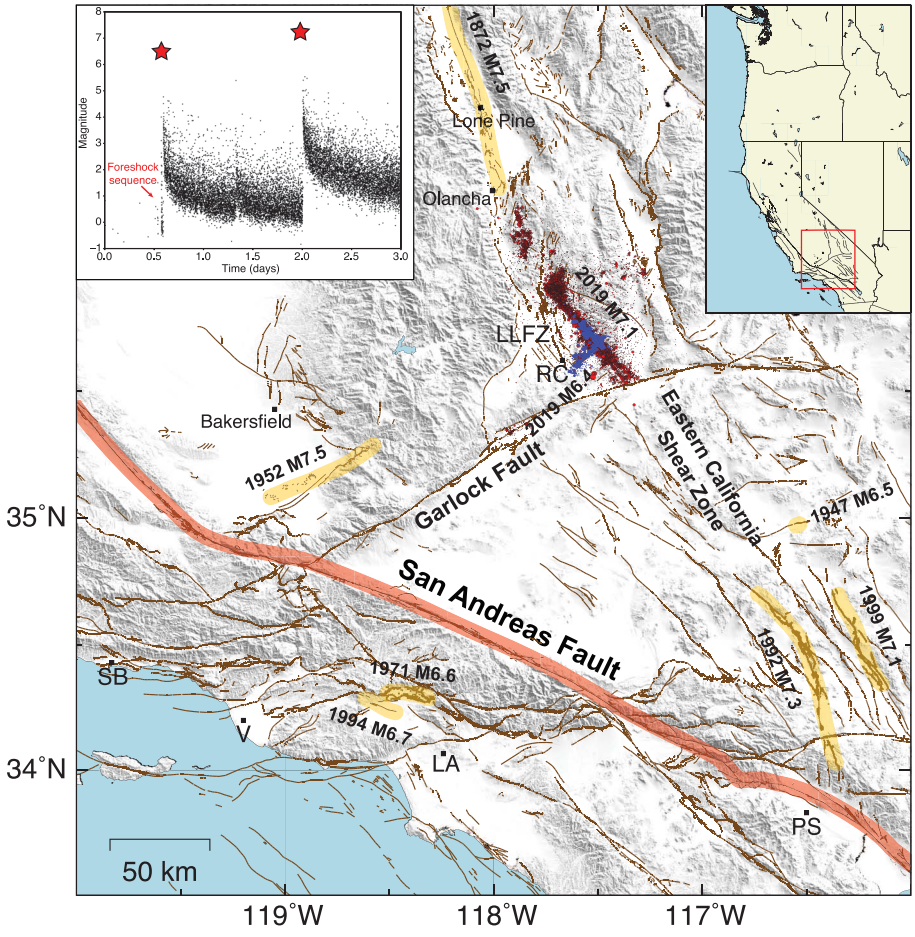

Fig. 1. Overview of study area. Mapped faults are indicated in brown. Ridgecrest sequence epicenters are shown as blue dots for time period up to the M_w 7.1 mainshock and as red dots following the mainshock. Santa Barbara, Los Angeles, Ventura, Palm Springs, and Ridgecrest and the LLFZ are denoted SB, LA, V, PS, RC, and LLFZ, respectively. Inset shows magnitude-time evolution of the first three days of the sequence. Note the catalog incompleteness during the first few days after the largest events. The M_w 6.4 event was preceded by a prominent foreshock sequence.

regions of many other earthquakes (*15*). Slip in the model has a maximum depth that is close to that of the seismicity (~10 km). We found that both strands of the bifurcation ruptured for about 12 km, terminating less than 5 km from the Garlock fault. These observations agree with the extent of seismicity. There is evidence from the seismicity for one or more additional subparallel faults on the southwest side of these two (Fig. 2).

The faults that ruptured during the M_w 7.1 event appear to be distinct from those that produced the M_w 6.4 event, which likely indicates that no fault ruptured the same area twice. The initial portion of the M_w 6.4 rupture propagated to the northwest about 6 km and terminated about 4 km from the eventual M_w 7.1 hypocenter (Fig. 4 and fig. S7). This 4-km gap was progressively filled by a series of moderate-sized earthquakes in the 34 hours after the M_w 6.4 event, which suggests that this portion of the fault acted as a barrier through which the M_w 6.4 rupture was unable to propagate (Fig. 4 and fig. S7). However, from the DPM (Fig. 3B), it is clear that this 4-km-long segment did rupture the surface at some point during the sequence, which most likely occurred during the M_w 7.1 event. The M_w 7.1 event appears to have been triggered because steady seismic activity eroded away this barrier. Furthermore, from our modeling of the source process of the M_w 6.4 event, this foreshock either jumped across the primary fault that failed during the M_w 7.1 event or ruptured through it in an orthogonal direction, yet it was somehow unable to trigger this large fault at that time. Instead, the M_w 7.1 event nucleated more than 10 km away from this intersection after being weakened by a series of M_w >4 earthquakes over 34 hours. The dynamic rupture conditions that could allow for such a scenario are not clear.

In addition to direct aftershocks that occurred in the LLFZ, the Ridgecrest sequence initiated three sizable earthquake swarms. One swarm

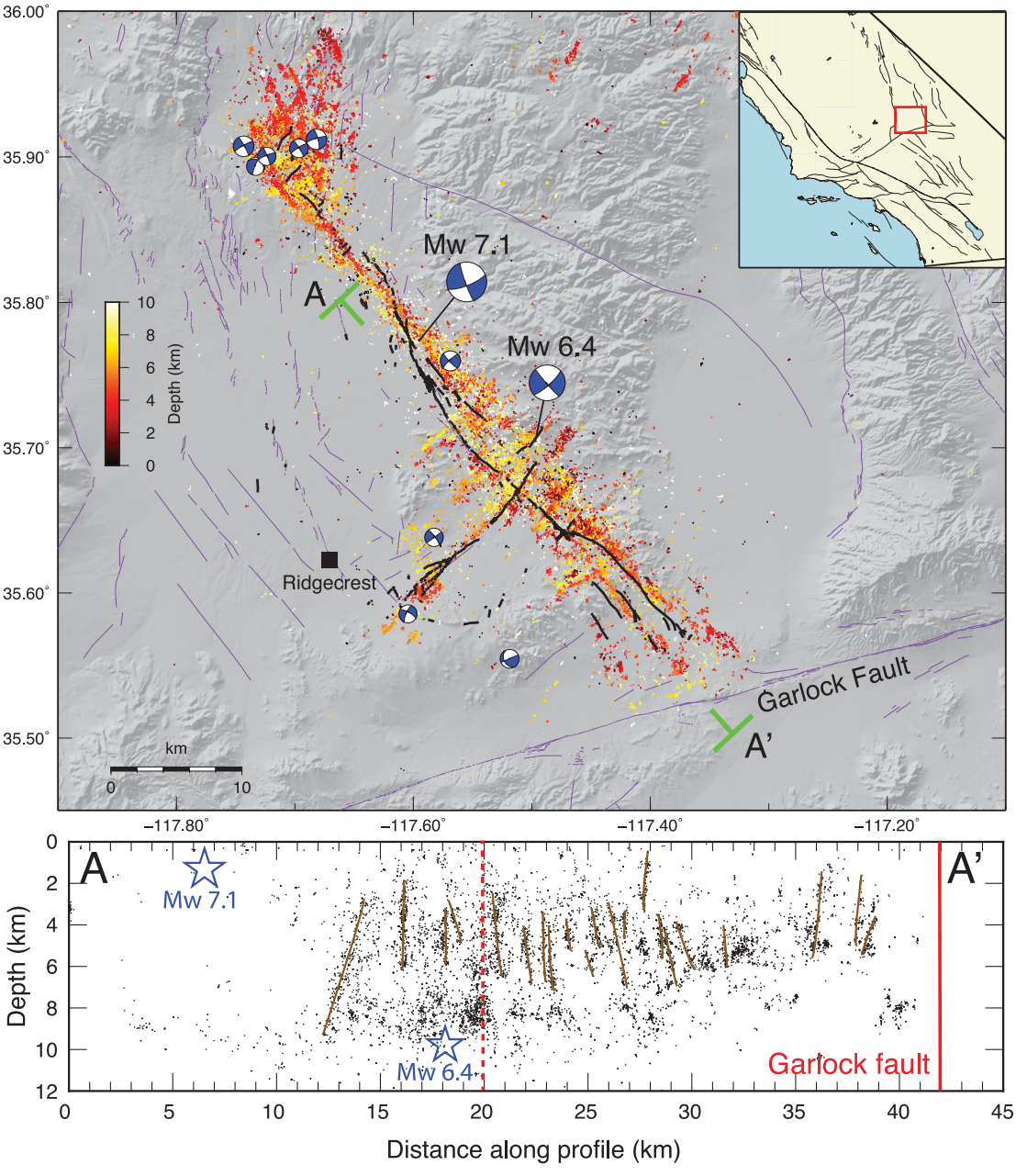

Fig. 2. Map view of Ridgecrest seismicity. Black lines indicate the surface trace of the fault (*31*), and purple lines indicate quaternary faults. Events with M_w of >4.5 are indicated by focal mechanisms (*32*). The fault network exhibits multiscale orthogonal faulting throughout the region, with a bifurcation to the southeast and horsetail faulting at the northwest terminus. The lower panel shows a seismicity cross section for events within 1 km of A-A′ with interpreted faults drawn shown as brown lines. At least 20 orthogonal faults cut through this profile. The dashed red line indicates the surface trace of southwest-trending fault that ruptured in the M_w 6.4 event.

was activated on the Garlock fault by the M_w 6.4 event and locates in a pull-apart structure about 50 km southwest of the Ridgecrest sequence (fig. S9). More than 4000 events with an M of >0 occurred in this swarm during the first 3 weeks, the largest of which was M_L 3.2 (fig. S9). This area has seen only minor seismic activity over the past several decades. Another swarm began north of the Coso geothermal field (Fig. 1), where similar behavior was observed following the Landers earthquake (*16*), with a 15-km gap over the geothermal production area (*17*). A third swarm was triggered in Panamint Valley.

On the section of the Garlock fault south of the rupture terminus of the Ridgecrest mainshock, InSAR data reveal an ~30-km zone of left-lateral, triggered, shallow creep (Fig. 6). The largest surface offset is around 20 mm of relative motion in the satellite line-of-sight direction, directly on the bearing of the M_w 7.1 rupture. The narrow extent of the deformation field suggests that the creep is confined to the upper few hundred meters. This creep is similar to shallow creep induced by other major earthquakes (*18*). Although the Garlock fault has been seismically quiescent during the historic period, it has hosted numerous large earthquakes during the previous several thousand years (*19*). However, previous geodetic measurements have shown no measurable creep on the Garlock fault (*20*).

Discussion

Most of our knowledge about the structural architecture of fault zones comes from observations made on the surface, which consist primarily of geological mapping of faults and geodetic observations of coseismic deformation. At depth, our understanding of properties such as the geometry of fault zones is far less complete, with most evidence suggesting a general tendency for structural complications like damage zones to localize and simplify with depth (*21*). For the Ridgecrest earthquakes, we find that nearly every aspect of the surface geometry persists at depth, including the bifurcation of the M_w 7.1 rupture to the southeast, the horsetail faulting

at the northwest terminus, the multiple segments that ruptured during the M_w 6.4 rupture, and the rampant orthogonal faulting. Below a 6-km depth, the main faults that ruptured during the M_w 7.1 event may become slightly more planar. The smaller orthogonal faults produced events primarily with M of <3, whereas events with M of >3 are mostly associated with the largest structures (fig. S15). These results show that precisely relocated seismicity catalogs are of sufficient resolution to constrain fault geometry and even some aspects of the rupture process at depth.

Orthogonal faulting occurring over a large region, at multiple length scales, implies that this is a primary characteristic of this fault zone. The smallest of these structures, having a length of 1 km or less, are probably being slowly generated as part of the ongoing formation of this young fault zone. Assuming a Mohr–Coulomb failure criterion, if two orthogonal planes are equally favorable, then the coefficient of friction must be close to zero, implying that the rocks are held together by cohesive strength alone (*22*). Alternatively, numerical studies have shown that cross-faults can be produced as a dynamic rupture effect near rupture edges (*23*). If a fault zone has widespread cross-faulting, the geometry could have a major influence on the earthquake rupture process, because at any point in time there will be many potential pathways to sustain the rupture propagation, thereby facilitating the occurrence of multifault ruptures.

The Ridgecrest sequence has many similarities with the 1987 Superstition Hills sequence (*24*), which also exhibited prominent orthogonal faulting and had an M_w 6.2 foreshock followed by a M_w 6.6 mainshock. In that sequence, the two largest events formed an L-shaped geometry, similar to the faults that ruptured during the Ridgecrest M_w 6.4 event. More generally, however, orthogonal faulting is present across much of southern California as well as Japan (*25–28*) and was also prominent in the 2012 Indian Ocean sequence (*29*).

The highly segmented nature of the Ridgecrest earthquakes suggests that the rupture process during these events could be more of a cascading phenomenon than a single continuous rupture front propagating along a fault. This behavior would depend at least partly on whether the faults are physically connected at depth. In a cascading rupture process, estimates of the average rupture velocity could be biased because the time of slip initiation for each segment is not a smoothly varying function of space and time. More important, however, is that the physics of the rupture process is entirely different in a cascading model, with ruptures potentially being modulated or driven by the seismic waves.

In the Ridgecrest sequence, at least 20 faults with a length of ~2 km or larger ruptured, with countless smaller faults that likely slipped too. Many of these ruptured the surface, while others are only visible at depth. The Ridgecrest earthquakes are the latest large crustal earthquakes to exhibit multifault ruptures (*1–5*), which several decades ago were viewed as unlikely or outright impossible (*1*). Today, with the available resolution, this phenomenon appears to be more common than not. The persistence of multifault ruptures indicates that the

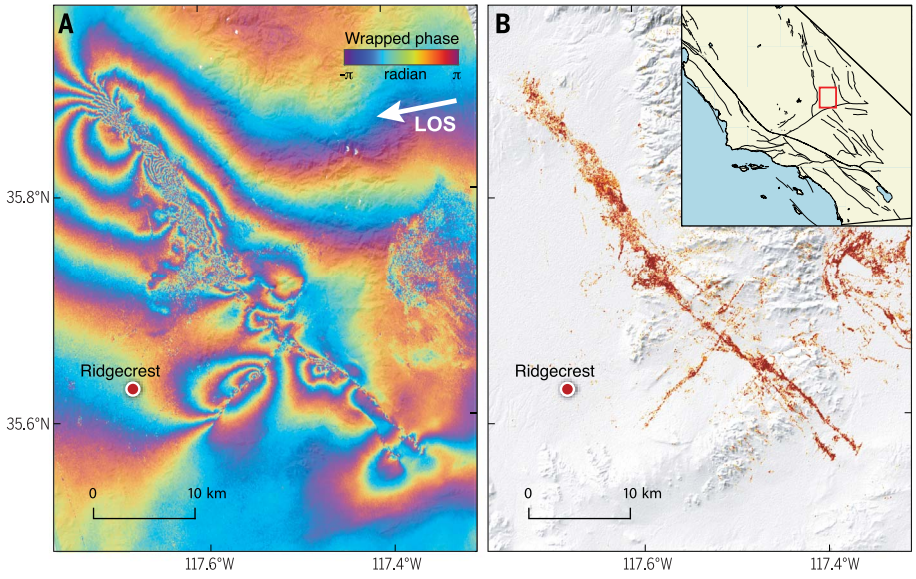

Fig. 3. Interferogram and DPM. (**A**) Coseismic interferogram derived from the ALOS-2 SAR image pair (2018-04-16 and 2019-07-08), showing the locations of surface ruptures. The line of site (LOS) is from ground to satellite. (**B**) DPM derived from coherence loss between pre- and postseismic Sentinel-1 SAR data. Darker colors indicate greater coherence losses.

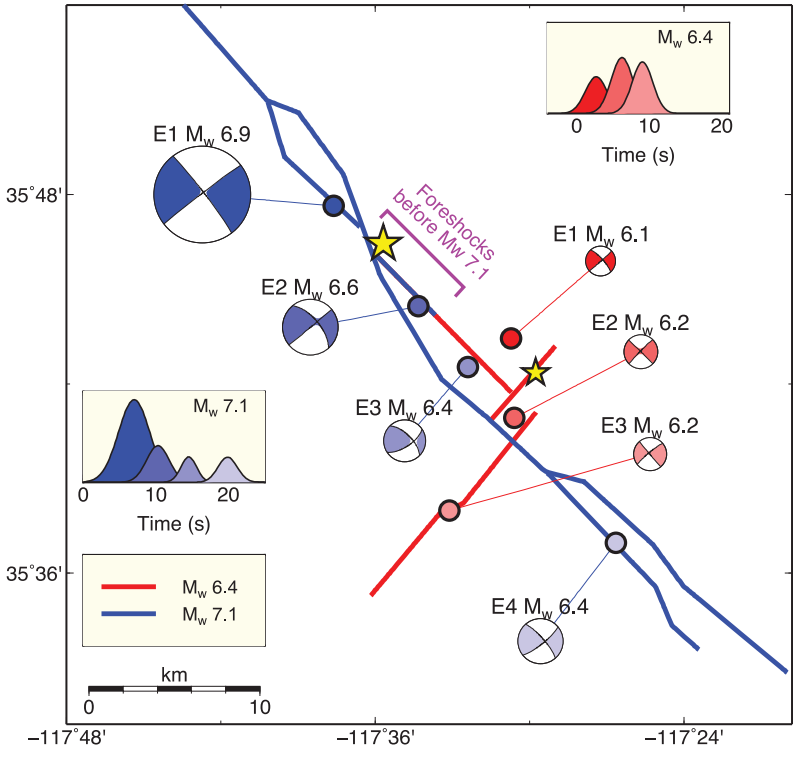

Fig. 4. Kinematic summary of rupture processes. The M_w 6.4 foreshock ruptured three main faults. This event was followed by foreshock activity along a northwest-trending fault and eventually triggered the M_w 7.1 event. The mainshock had four main subevents and ruptured bilaterally. Both events have very slow rupture velocities of ~2 km/s.

phenomenon is a critical element of the physics of earthquakes.

Furthermore, the regular occurrence of multi-fault ruptures has fundamental implications for seismic hazard assessment. Accounting for all possible combinations of faults that could activate simultaneously during a single event or sequence is challenging, if not functionally impossible. This task is made even more difficult by the fact that, as demonstrated by the Ridgecrest sequence, our database of large faults in California is still incomplete, and the concept

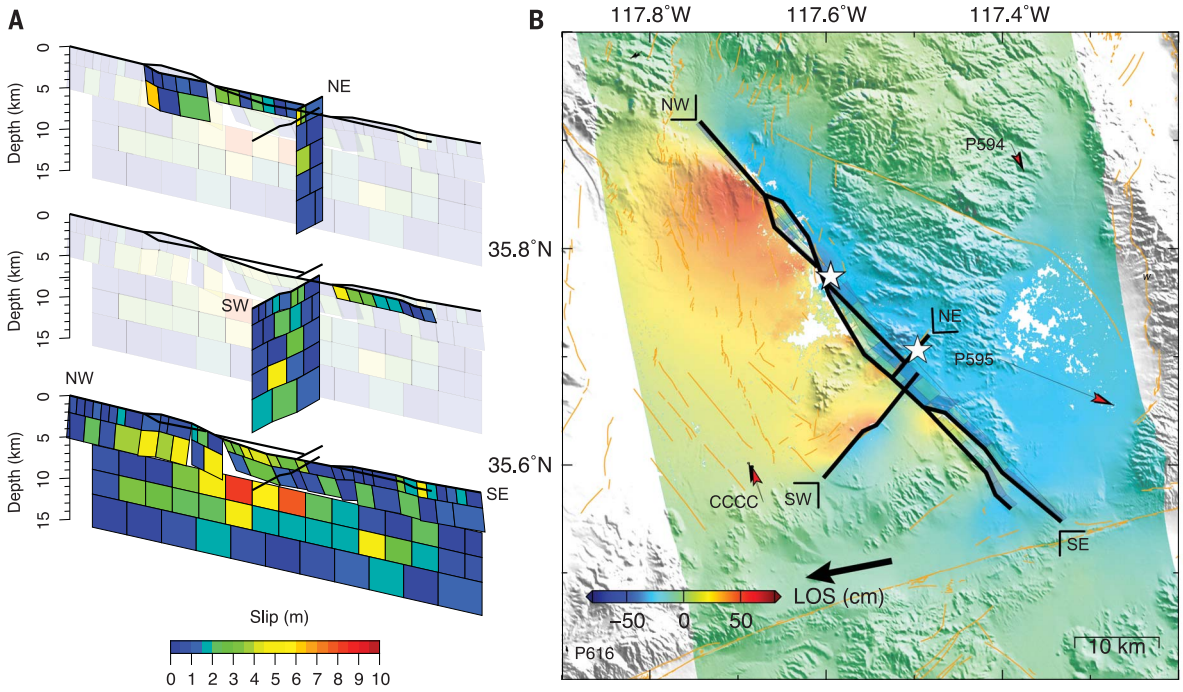

Fig. 5. Static inversion of geodetic data. (**A**) Mean slip model of the Ridgecrest sequence, including the slip contribution from the M_w 6.4 and M_w 7.1 events. (**B**) Black lines show the fault geometries used in the slip. Arrows indicate the data (black) and model prediction (red) of nearby GPS offsets. The color map indicates the displacements in the unwrapped ALOS2 ascending track 65 coseismic interferogram along the corresponding line-of-sight (LOS) direction (black arrow). Model predictions and data residuals are provided in the supplementary materials (*11*).

Fig. 6. Summary of triggered creep on the Garlock fault. Step function fit at the coseismic time for Sentinel 1, ascending track 64 InSAR time series, combined with gradient shading of the same field. The gradient shading reveals zones of surface offset along the Garlock fault. Fault perpendicular profiles reveal offset of up to 20 mm in the line-of-sight direction, while the width of the deformation profiles suggest that offset on the fault is confined to shallow depths.

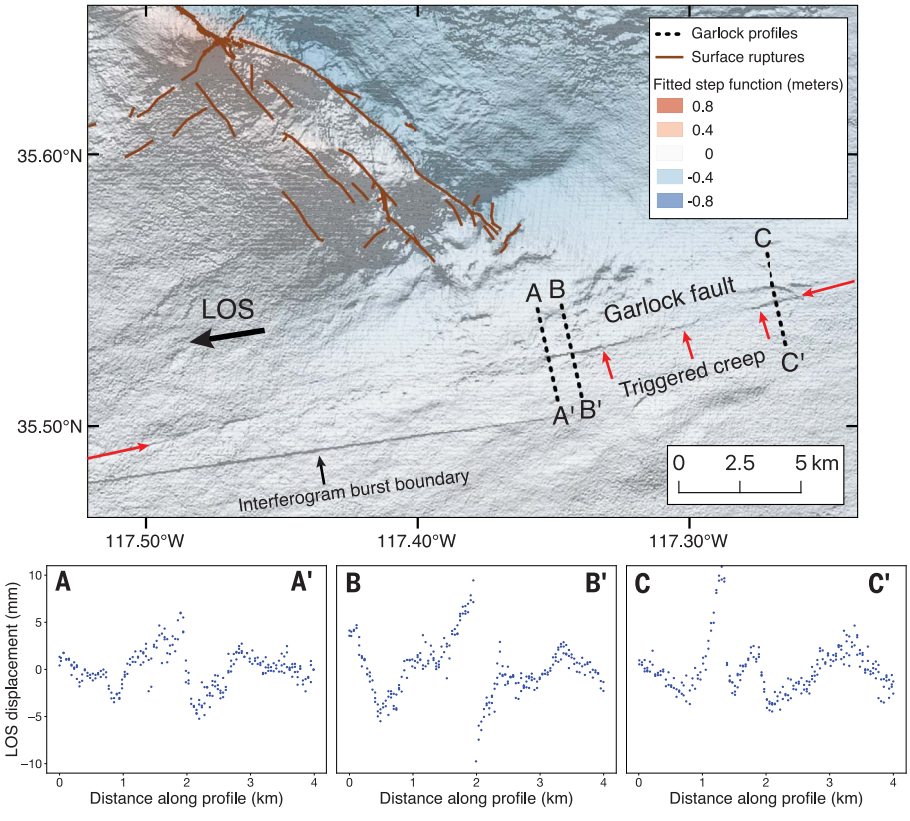

of how faults are defined should be revisited. Magnitude estimates of historical earthquakes from paleoseismology could therefore be biased downward for many such multifault ruptures, while also exposing the potential for incorrectly splitting a single complex rupture into multiple smaller ones. As Fig. 1 shows, although the San Andreas fault may be the single largest source of hazard in southern California, nearly all large earthquakes since the 1906 San Francisco earthquake, over a century ago, have not occurred on the San Andreas fault, and many have been complex multifault ruptures.

Conclusions

The 2019 Ridgecrest sequence brought to an end the long earthquake silence in California. These events occurred within an immature fault zone and activated many orthogonal structures with lengths ranging from 1 km to more than 10 km. The largest events each ruptured multiple faults, a characteristic that has been repeatedly observed for large crustal earthquakes in recent years. Such scenarios are difficult to forecast for seismic hazard assessment. The rupture of the Ridgecrest mainshock terminated only a few kilometers from the Garlock fault, yet only aseismic creep was triggered at the closest section of the fault. Far to the southwest, a sizable swarm ensued, whereas triggered seismic activity on the entire eastern portion of the Garlock fault was negligible. At such close proximity to the mainshock rupture, the stress changes imparted by the mainshock are substantial. The last major earthquake occurred ~400 to 500 years ago (*30*). Future investigations that integrate the observed phenomena on the Garlock fault with geologic and geodetic observations will be important for understanding its contribution to seismic hazard in the Eastern California shear zone.

REFERENCES AND NOTES

1. K. Sieh *et al*., *Science* **260**, 171–176 (1993).
2. M. Simons, Y. Fialko, L. Rivera, *Bull. Seismol. Soc. Am.* **92**, 1390–1402 (2002).
3. D. Eberhart-Phillips *et al*., *Science* **300**, 1113–1118 (2003).
4. S. J. Wei *et al*., *Nat. Geosci.* **4**, 615–618 (2011).
5. I. J. Hamling *et al*., *Science* **356**, eaam7194 (2017).
6. E. Hauksson *et al*., *Seismol. Res. Lett.* **66**, 54–60 (1995).
7. C. B. Amos *et al*., *GSA Bull.* **125**, 1187–1202 (2013).
8. G. A. Davis, B. C. Burchfiel, *Bull. Geol. Soc. Am.* **84**, 1407–1422 (1973).
9. Y. Fialko, M. Simons, *J. Geophys. Res. Solid Earth* **105** (B9), 21781–21793 (2000).
10. E. K. Haddon, C. B. Amos, O. Zielke, A. S. Jayko, R. Bürgmann, *Geochem. Geophys. Geosyst.* **17**, 2239–2269 (2016).
11. Materials and methods are described in the supplementary materials.
12. S.-H. Yun *et al*., *Seismol. Res. Lett.* **86**, 1549–1556 (2015).
13. D. I. Doser, H. Kanamori, *J. Geophys. Res. Solid Earth* **91** (B1), 675–688 (1986).
14. E. Hauksson, *Geophys. J. Int.* **186**, 82–98 (2011).
15. N. Wetzler, T. Lay, E. E. Brodsky, H. Kanamori, *Sci. Adv.* **4**, eaao3225 (2018).
16. D. P. Hill *et al*., *Science* **260**, 1617–1623 (1993).
17. Q. Zhang *et al*., *Geophys. Res. Lett.* **44**, 726–733 (2017).
18. M. Wei, D. Sandwell, Y. Fialko, R. Bilham, *Geophys. Res. Lett.* **38**, n/a (2011).
19. J. F. Dolan, L. J. McAuliffe, E. J. Rhodes, S. F. McGill, R. Zinke, *Earth Planet. Sci. Lett.* **446**, 123–136 (2016).
20. X. Tong, D. T. Sandwell, B. Smith-Konter, *J. Geophys. Res. Solid Earth* **118**, 369–389 (2013).
21. Y. Ben-Zion, C. G. Sammis, *Pure Appl. Geophys.* **160**, 677–715 (2003).
22. C. H. Scholz, *The Mechanics of Earthquakes and Faulting* (Cambridge Univ. Press, 2019).
23. S. Q. Xu, Y. Ben-Zion, *Geophys. J. Int.* **193**, 304–320 (2013).
24. K. W. Hudnut, L. Seeber, J. Pacheco, *Geophys. Res. Lett.* **16**, 199–202 (1989).
25. W. Thatcher, D. P. Hill, *Geology* **19**, 1116–1120 (1991).
26. E. Fukuyama, *Earth Planets Space* **67**, 38 (2015).
27. Z. E. Ross, E. Hauksson, Y. Ben-Zion, *Sci. Adv.* **3**, e1601946 (2017).
28. Z. E. Ross *et al*., *Geophys. Res. Lett.* **44**, 8260–8267 (2017).
29. L. Meng *et al*., *Science* **337**, 724–726 (2012).
30. C. Madden Madugo, J. F. Dolan, R. D. Hartleb, *Bull. Seismol. Soc. Am.* **102**, 2282–2299 (2012).
31. K. J. Kendrick *et al., Southern California Earthquake Center Annual Meeting Proceedings* (SCEC, 2019), contribution 9779.
32. SCEDC, Data are available from the Southern California Seismic Network (https://doi.org/10.7914/SN/CI), operated by the California Institute of Technology and the United States Geological Survey (2013).

ACKNOWLEDGMENTS

The ALOS-2 original data are copyrighted by JAXA and provided under JAXA RA6 PI projects P3278 and P3360. The Copernicus Sentinel-1 data were provided by the European Space Agency (ESA) and contain modified Copernicus data 2019, processed by ESA, Caltech, and NASA/JPL. **Funding:** E.H. received support from USGS/NEHRP grant G19AP00035 and NSF awards EAR-1550704 and EAR-1818582; Z.Z. and Z.J. received support from USGS grant G19AP00030. Part of the research was carried out at the Jet Propulsion Laboratory, California Institute of Technology, under a contract with the National Aeronautics and Space Administration. This material is based on services provided by the GAGE Facility, operated by UNAVCO, Inc., with support from the National Science Foundation and the National Aeronautics and Space Administration under NSF Cooperative Agreement EAR-1724794. **Author contributions:** Z.E.R. performed the template matching and seismicity relocation. E.H. calculated three-dimensional earthquake locations. M.S. and B.I. performed the slip inversion. Z.J., X.W., and Z.Z. performed the subevent modeling. E.J.F. and O.L.S. performed the InSAR data processing. M.Z. determined offset fields for the InSAR data. S.-H.Y. and J.J. produced the DPMs. Z.L. and A.W.M. processed the GPS data. O.L.S. performed the Garlock fault creep analysis and smoothed seismicity plots. All authors contributed to writing the manuscript. **Competing interests:** A.W.M. is a member of the UNAVCO Geodetic Data Services Advisory Committee. **Data and materials availability:** All seismic data used are publicly available from the Southern California Earthquake Data Center and the IRIS DMC. GPS data are available from Network of the Americas (NOTA) and UNAVCO. The seismicity catalog produced in this study is publicly available from the Southern California Earthquake Data Center.

SUPPLEMENTARY MATERIALS

science.sciencemag.org/content/366/6463/346/suppl/DC1
Materials and Methods
Figs. S1 to S19
Tables S1 to S4
References (*33*–*61*)

5 August 2019; accepted 23 September 2019
10.1126/science.aaz0109

Hierarchical interlocked orthogonal faulting in the 2019 Ridgecrest earthquake sequence

Zachary E. Ross, Benjamín Idini, Zhe Jia, Oliver L. Stephenson, Minyan Zhong, Xin Wang, Zhongwen Zhan, Mark Simons, Eric J. Fielding, Sang-Ho Yun, Egill Hauksson, Angelyn W. Moore, Zhen Liu and Jungkyo Jung

Science **366** (6463), 346-351.
DOI: 10.1126/science.aaz0109

Many ruptures across many scales

The period of seismic quiescence in Southern California was rudely interrupted by the Ridgecrest earthquake sequence in July 2019. Ross *et al.* mapped the slip sequences during the magnitude 6.4 and 7.1 earthquakes that shook the region. They found that ruptures of a few larger, but many smaller, faults occurred during both earthquakes. The Ridgecrest sequence calls for rethinking seismic hazard, as multifault ruptures are not usually considered when assessing seismic risk.

Science, this issue p. 346